SCIEPublish

Article

Experimental Study on Cold Plasma Jet (CPJ) Assisted Micro-Milling of 30CrMnSiNi2A

Ziheng Wang [1], Wei Yang [2], Zhenjing Duan [1], Shuaishuai Wang [1], Yuheng Li [1], Yuyang Zhou [1], Jiyu Liu [3], Jinlong Song [1] and Xin Liu [1,*]

[1] State Key Laboratory of High-Performance Precision Manufacturing, Dalian University of Technology, Dalian 116024, China; wzh93123456@gmail.com (Z.W.); zhenjing456@126.com (Z.D.); wangshuais2022@126.com (S.W.); liyhh1996@163.com (Y.L.); zyuyang12@163.com (Y.Z.); songjinlong@dlut.edu.cn (J.S.)

[2] Shenyang Aircraft Corporation, Shenyang 110850, China; yangwei343@sina.com (W.Y.)

[3] College of Mechanical and Electrical Engineering, Northeast Forestry University, Harbin 150000, China; liujiyu19940802@163.com (J.L.)

* Corresponding author. E-mail: xinliu@dlut.edu.cn (X.L.)

Received: 30 September 2024; Accepted: 25 October 2024; Available online: 29 October 2024

ABSTRACT: As a typical high-performance alloy, the excellent mechanical properties and stringent processing requirements of 30CrMnSiNi2A high-strength steel pose great challenges to high-quality and efficient processing. Currently, researchers have proposed methods such as improving cutting tool performance, minimal quantity lubrication (MQL), and applying external energy field to assist processing. However, due to the unregulated material properties, the further improvement of surface quality is limited, and there are problems of phase change and thermal damage in laser processing. Cold plasma jet (CPJ) is rich in active particles and has a low macroscopic temperature. It can effectively regulate material properties without causing serious surface damage. Therefore, a new 30CrMnSiNi2A machining approach adopting CPJ is proposed to improve the cutting process. The mechanism of its action on material properties and cutting process is revealed based on single-grain diamond scratching tests and micro-milling tests. The results show that CPJ can promote material fracture and improve material removal efficiency. The material removal efficiency R at 400 mN is increased from 0.433 before treatment to 0.895. Under the optimal processing parameters (feed speed V_f = 800 μm/s, spindle speed n = 40,000 rpm, and milling depth a_p = 5 μm), compared with dry micro-milling, the cutting forces F_z, F_x and F_y in CPJ-assisted micro-milling are reduced by 26.5%, 24.8% and 31.3%, respectively. The surface roughness Sa is reduced by 19.3%, and the phenomena of plastic flow and burr are suppressed. The CPJ-assisted machining process proposed in this paper can regulate the material properties to improve the cutting process without causing serious damage to the material, providing a new approach for achieving high-quality and efficient processing of 30CrMnSiNi2A.

Keywords: Cold plasma jet; 30CrMnSiNi2A; Micro-milling; Scratching; Cutting force; Surface quality

1. Introduction

As an important high-performance alloy, 30CrMnSiNi2A high-strength steel is widely used in shipbuilding, military equipment, aerospace and other fields due to its high strength, high toughness and good wear resistance [1–4]. In addition, with the rapid development of science and technology and industrial manufacturing, higher requirements have been proposed for the machining process of parts. For example, the dimensional error of aircraft engine parts is required to be less than 10 μm, and the surface roughness Ra is less than 0.5 μm [5]. When processing high-performance alloys represented by 30CrMnSiNi2A, the large cutting force and high cutting temperature cause severe tool wear, and the good toughness causes serious burrs [6]. Therefore, these excellent mechanical properties and stringent processing requirements pose new challenges to the high-quality and efficient processing of high-performance alloys.

To address these challenges, researchers have proposed methods such as improving cutting tool performance [7–11], minimal quantity lubrication (MQL) [12–16], applying external energy field to assist processing [17–21] and multi-energy field coupling [22–25]. For the methods to improve cutting tool performance, Niu et al. [7] adopted coated tools

https://doi.org/10.70322/ism.2024.10017

to mill 30CrMnSiNi2A and studied tool wear during processing. They found that compared with chemical vapor deposition (CVD), coated tools obtained by physical vapor deposition (PVD) exhibited better performance, and their wear forms were adhesive wear and coating peeling. Deng et al. [8] performed turning tests on 45# hardened steel using microporous textured tools and solid lubricants and found that the friction coefficient of the tool-chip interface was greatly reduced, thereby inhibiting tool wear. For the methods of MQL-assisted processing, Li et al. [12] explored the effects of different types of vegetable oils on MQL-assisted grinding of GH4169. The results suggested that palm oil was the optimal base oil for MQL grinding, with a grinding temperature of 119.6 °C, and an energy ratio coefficient of 42.7%. For the methods of applying external energy field assisted processing, You et al. [17] conducted a study on ultrasonic-assisted grinding of single crystal nickel-based alloys. The results showed that ultrasonic vibration could transform the material removal mode from ploughing and squeezing to shearing removal, and the grinding force and grinding temperature were reduced by 63.2% and 46.7%, respectively. Huang et al. [20] discovered that laser could reduce the hardness and elastic modulus of the material and improve the material removal efficiency in the test of diamond tool turning die steel. Meanwhile, the tool life increased by 29% and the surface roughness *Ra* could reach 12 nm. For the methods of multi-energy field coupling assisted processing, Du et al. [22] proposed a new process for laser coupled ultrasonic assisted turning of SiCp/Al6061 composite materials and found that multi-energy fields could better control chip shape and inhibit tool wear. The surface roughness *Sa* of different composite materials was less than 30 nm.

Although the above methods can improve cutting conditions and inhibit tool wear to a certain extent, the material properties have not been effectively regulated, which limits further improvements in surface quality and machining efficiency. And there are phase change and thermal damage problems in laser-assisted processing. Therefore, there is an urgent need for a processing method that can effectively regulate material properties, while not causing significant damage to the material, to achieve high-quality and efficient ultra-precision processing of 30CrMnSiNi2A. Cold plasma jet (CPJ) contains a large number of active particles such as ions, electrons and excited state atoms [26–28], with a low macroscopic temperature. These active particles can effectively regulate material properties without causing serious surface damage. Currently, CPJ has been used in the auxiliary processing of a variety of difficult-to-cut materials. Some scholars [29–31] proposed a new process for CPJ-assisted polishing of hard and brittle materials such as single crystal silicon, diamond and AlN ceramics. The results implied that the hardness of the material modified by CPJ was reduced, and efficient and non-destructive removal of the material could be achieved. We [32–37] have also conducted research on CPJ-assisted micro-milling of difficult-to-cut materials such as nickel-based high-temperature alloys, titanium alloys, single-crystal silicon, amorphous alloys and aluminum-lithium alloys. The results demonstrated that CPJ could improve the cutting process and surface quality by modulating the properties of difficult-to-cut materials. However, for 30CrMnSiNi2A, the relevant research on the effect of CPJ on its material properties and cutting process has not been reported.

In this paper, the influence mechanism of CPJ on material properties and cutting process of 30CrMnSiNi2A was systematically investigated. Firstly, the influence of CPJ on material removal behavior was explored through a single-grain diamond scratching test. On this basis, the orthogonal micro-milling test was carried out to determine optimal processing parameters. Finally, the micro-milling test was carried out under different processing conditions. Cutting force, surface roughness and surface micromorphology were measured to explore the influence of CPJ on the cutting process of 30CrMnSiNi2A high-strength steel. The results indicated that CPJ could effectively adjust the machinability of 30CrMnSiNi2A, providing a new approach to meet the demands for its application in shipbuilding, military equipment, aerospace and other fields.

2. Materials and Methods

2.1. Materials

The material used in the test was 30CrMnSiNi2A high-strength steel bar, and the test sample with a size of Φ45 mm × 3 mm was obtained by cutting. The chemical composition and physical performance parameters of the material are shown in Tables 1 and 2.

Table 1. Chemical composition content (w.t.%) of 30CrMnSiNi2A.

Elements	Cr	Mn	Si	Ni	Cu	C	Fe
Content	0.9–1.2	1–1.3	0.9–1.2	1.4–1.8	0.25	0.27–0.34	Bal.

Table 2. Physical performance parameters of 30CrMnSiNi2A.

Parameters	Unit	Value
Elastic modulus	GPa	211
Hardness	HRC	≥45
Yield strength	MPa	≥1375
Tensile strength	MPa	≥1620
Elongation		≥10%
Impact Toughness	$J \cdot cm^{-2}$	≥69

2.2. Experimental Devices

As shown in Figure 1, the experimental device mainly consisted of a single-grain diamond scratching device, a micro-milling machine and a CPJ generating device. The single-grain diamond scratching device (Micro/nano-Scratcher-1000-V, China) was developed by Jilin University [38]. The motion resolution in the *x*, *y*, and *z* directions was 250 nm, 250 nm, and 5 nm, respectively. The load resolution was 30 μN, and the scratching speed was 1–100 μm/s. It could achieve precise scratching of materials under a large load range of 1–1000 mN. The test indenter was an HV-6 Vickers indenter with a cross edge of 500 nm, which was performed with the edge facing forward during the scratching process. The maximum speed of the micro-milling machine spindle (EMSF-3060K, Nakanishi, Japan) was 60,000 r/min, and the spindle rotation accuracy was within 1 μm. The maximum feed of the feed platform (M-403, PI, Germany) in the *x*, *y*, and *z* directions was 100 mm, 100 mm, and 200 mm, respectively. The maximum feed speed in each direction was 10 mm/s, with a feed accuracy of 0.2 μm. The tool was a tungsten steel double-edged flat-end micro-milling cutter (CXF, China), with a helix angle of 60° and a diameter of 0.5 mm.

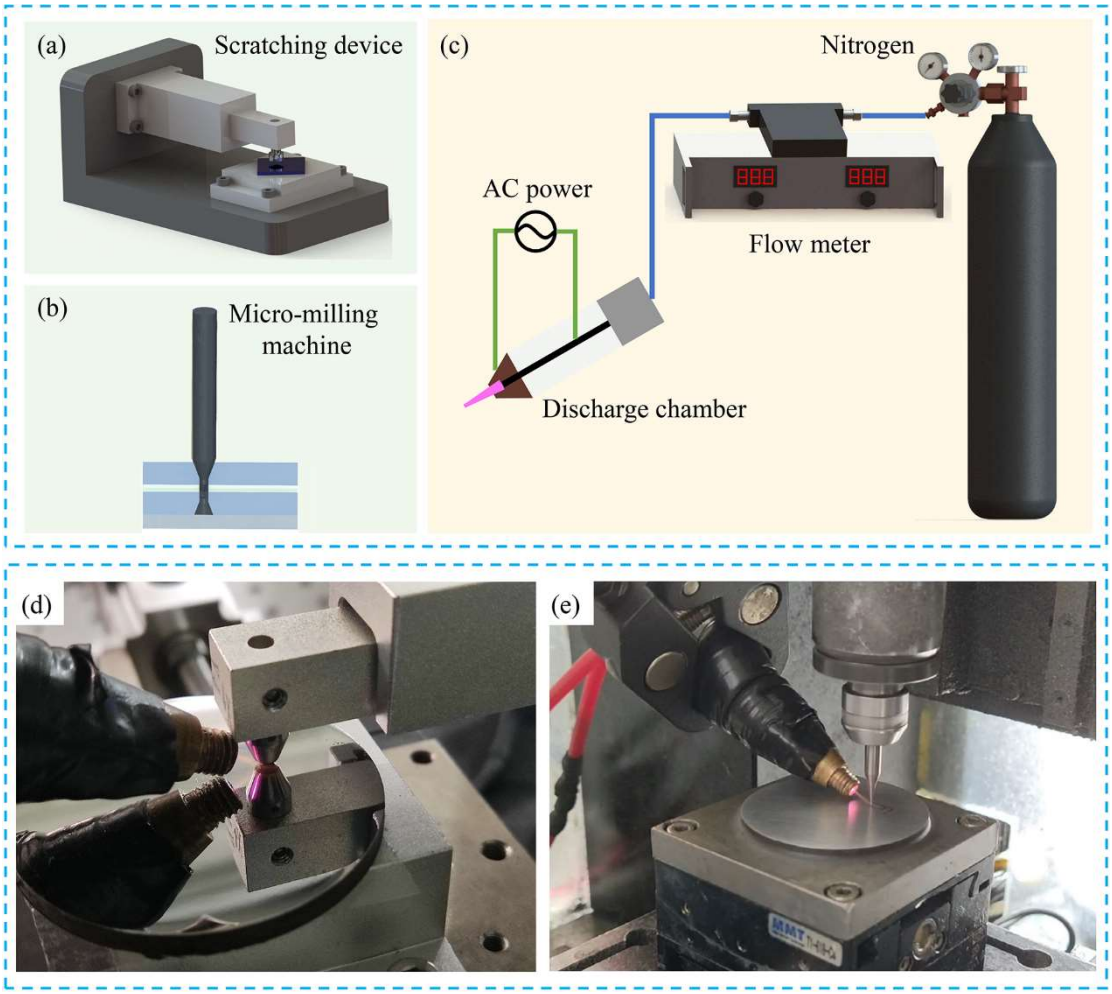

Figure 1. Schematic and physical drawings of the experimental devices: (**a**–**c**) schematic diagrams, (**a**) single-grain diamond scratching device, (**b**) micro-milling machine, (**c**) CPJ generating device; (**d**,**e**) physical drawings, (**d**) CPJ-assisted scratching device, (**e**) CPJ-assisted micro-milling device.

The CPJ generating device was mainly composed of a gas source, a flow meter, a low-frequency AC power supply and a discharge chamber. To achieve rapid modification of the material without affecting the micromorphology of the material surface, the CPJ was generated by bare electrode discharge. The discharge electrodes were composed of a high-voltage tungsten needle electrode and a low-voltage copper nozzle electrode, and there was no dielectric barrier such as a quartz tube between the electrodes. When nitrogen was introduced into the discharge chamber and a certain voltage was applied, a stable lavender CPJ could be generated. The temperature of the CPJ was about 30 ℃, and the length was about 15 mm, which could achieve rapid modification of the material processing area without causing serious thermal damages. The specific operating parameters are shown in Table 3. To avoid the influence of nitrogen gas flow on the machining process, nitrogen-assisted micro-milling experiments were carried out using the same gas pressure and flow rate in Table 3.

Table 3. The operating parameters of the CPJ generating device.

Parameter	Parameter Level
Working gas	99.999% Nitrogen
Gas pressure	0.4 MPa
Gas flow rate	12 L/min
Nozzle diameter	2.5 mm
AC power frequency	58.6 kHz
Discharge voltage	2.5 kV

2.3. Characterization Methods

To reveal the mechanism of CPJ on the material removal behavior of 30CrMnSiNi2A, a single-grain diamond scratching device was adopted to carry out scratching tests on samples before and after CPJ treatment. The 3D and 2D scratched morphologies were measured using a laser scanning confocal microscope (LSCM) (LEXT OLS5100, Olympus, Tokyo, Japan) and a scanning electron microscope (SEM) (Nova Nano SEM 450, FEI, Hillsboro, OR, USA). During the micro-milling process, a three-dimensional piezoelectric dynamometer (9256C1, Kistler, Winterthur, Switzerland), a charge amplifier (5080A, Kistler, Winterthur, Switzerland) and a data acquisition system (5697A, Kistler, Winterthur, Switzerland) were employed to collect the cutting forces in all directions. The sampling frequency of cutting force was 20 kHz. After processing, the surface roughness and micromorphology were measured and analyzed using a three-dimensional optical surface profiler (NewView9000, Zygo, Middlefield, NY, USA) and SEM. All experiments were repeated 3 times or more to avoid accidental errors.

3. Results and Discussion

3.1. The Effect of CPJ on Material Removal Behavior

For revealing the effect of CPJ on the removal behavior of 30CrMnSiNi2A, the material was subjected to variable-load and constant-load scratching tests using a single-grain diamond scratching test device. The load-time curve and scratched morphology were measured for the analysis of the removal process. Furthermore, the residual depth and removal efficiency were measured and calculated using the analysis software provided by LSCM, to compare the differences in residual depth and removal efficiency of the material before and after CPJ treatment. The specific parameters used in the scratching test are shown in Table 4.

Table 4. Processing parameters in scratching test.

Experiment	Load Mode	Loading Conditions	Scratching Length
Exp.1	Variable-load	0–1000 mN 5 μm/s	500 μm
Exp.2	Constant-load	100 mN 5 μm/s	100 μm
Exp.3	Constant-load	400 mN 5 μm/s	100 μm
Exp.4	Constant-load	700 mN 5 μm/s	100 μm
Exp.5	Constant-load	1000 mN 5 μm/s	100 μm

3.1.1. Variable-Load Scratching

The load-time curves and scratched micromorphologies of 30CrMnSiNi2A obtained by variable-load scratching are shown in Figure 2. F_N and F_L represent normal load and lateral load, respectively. With the increasing normal load, the material will go through three stages of sliding, ploughing and cutting during the scratching process. Under the condition of no CPJ treatment, as the increase of F_N, there was a slight fluctuation in the lateral force-time curve, which was related to the fracture phenomenon of the material with the increasing load (as shown in Figure 2(a1)). By contrast, the lateral force-time curve under CPJ-assisted scratching fluctuated more drastic, indicating that CPJ could promote the ductile fracture of the material to a certain extent, and the lateral force increased compared with that without CPJ treatment (as shown in Figure 2(b1)).

To further compare the differences in the removal process of materials with and without CPJ treatment, the micromorphologies of positions 1, 2, 3 and 4 corresponding to the load-time curve were measured, as shown in Figure 2(a2,b2). The results manifested that the width and depth of scratched groove increased with the increase of F_N, and there were material pileups and fractures on both sides of the groove with and without CPJ treatment. Obviously, the material had entered the cutting removal stage. This was because the loading rate in the scratching test was high, which weakened the sliding and ploughing stages of the material. In addition, the crack length induced by fracture under CPJ treatment was longer than that without CPJ treatment. The presence of shear bands (SBs) was observed at position 4 on the CPJ-assisted scratched surface, indicating that the material underwent highly concentrated shear deformation at this time. It was also consistent with the fluctuation phenomenon of the load-time curve under CPJ-assisted scratching, that is, CPJ could promote material fracture through the Rehbinder effect [39]. It was very beneficial for promoting chip breaking and reducing cutting force during processing. To reveal the effect of CPJ on the residual scratch depth and removal efficiency of the material, the constant-load scratching experiment was subsequently carried out.

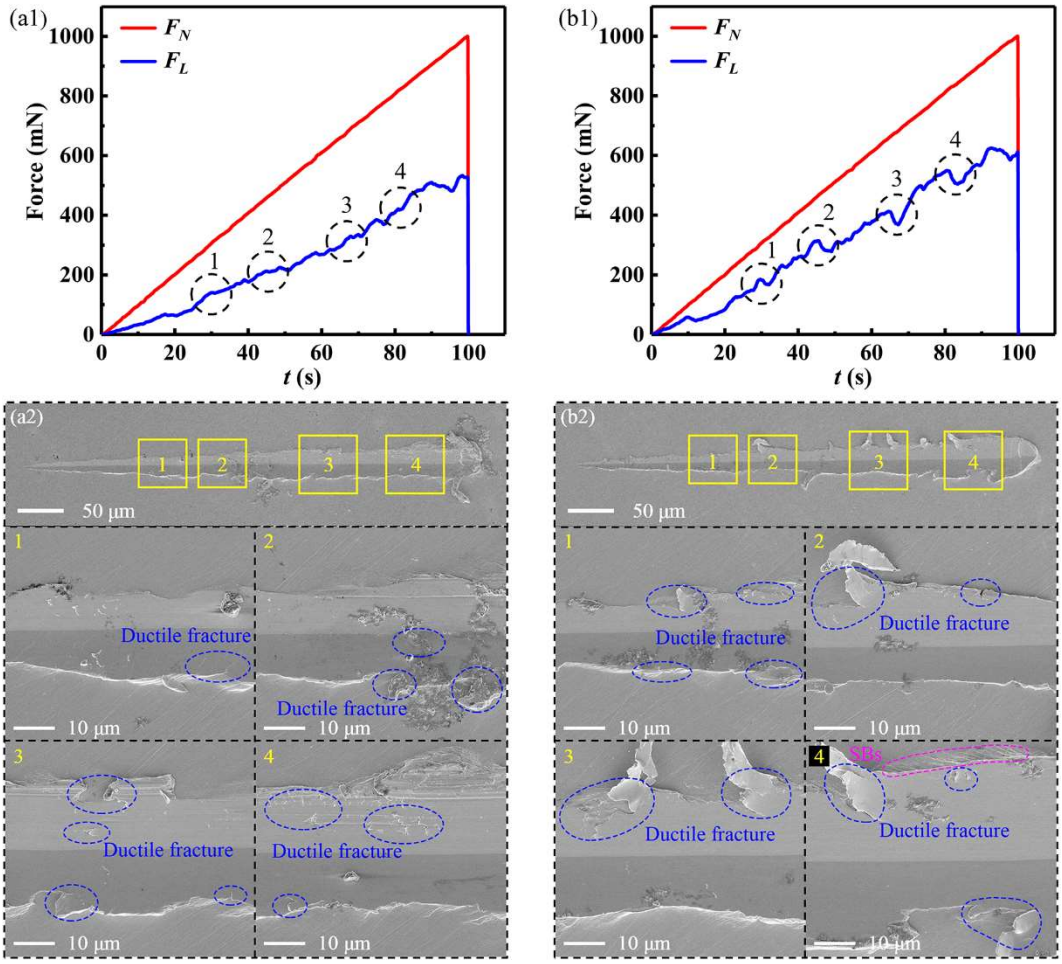

Figure 2. Load-time curves and scratched micromorphologies obtained by variable-load scratching of 30CrMnSiNi2A: (**a1**,**a2**) without CPJ treatment; (**b1**,**b2**) under CPJ treatment.

3.1.2. Constant-Load Scratching

On the basis of the variable-load scratching test, the constant-load scratching test was carried out on 30CrMnSiNi2A at F_N of 100 mN, 400 mN, 700 mN and 1000 mN, with a scratching speed of 5 μm/s. The obtained 2D and 3D scratched morphologies are shown in Figures 3 and 4. When the load was 100 mN, no ductile fracture occurred on the scratched surface with and without CPJ treatment, which was because the load was so low that the condition for material fracture was not reached (as shown in Figure 3(a1,b1)). When the load increased to 400 mN, the ductile fracture was observed on both surfaces, and the length and number of cracks on the scratched surface after CPJ treatment increased compared with those before treatment (as shown in Figure 3(a2,b2)). When the load was 700 mN, the length and number of cracks induced by CPJ-assisted scratching were also higher than those without CPJ assistance (as shown in Figure 3(a3,b3)). When the load reached the maximum value of 1000 mN, no obvious ductile fracture was observed on the scratched surface without CPJ treatment, while ductile fracture occurred on the scratched surface after treatment (as shown in Figure 3(a4,b4)). From the 3D scratched morphologies in Figure 4, it could be seen that the residual scratched depth after CPJ treatment was increased compared with that before treatment. In addition, there were more chip pileups at the scratched tail under F_N of 400 mN, 700 mN and 1000 mN, which might be attributed to the increase of material removal efficiency after CPJ treatment (as shown in Figure 4(a2–a4,b2–b4)). To further reveal the effect of CPJ on the residual scratched depth and removal efficiency, the residual depth and removal efficiency were measured and calculated subsequently.

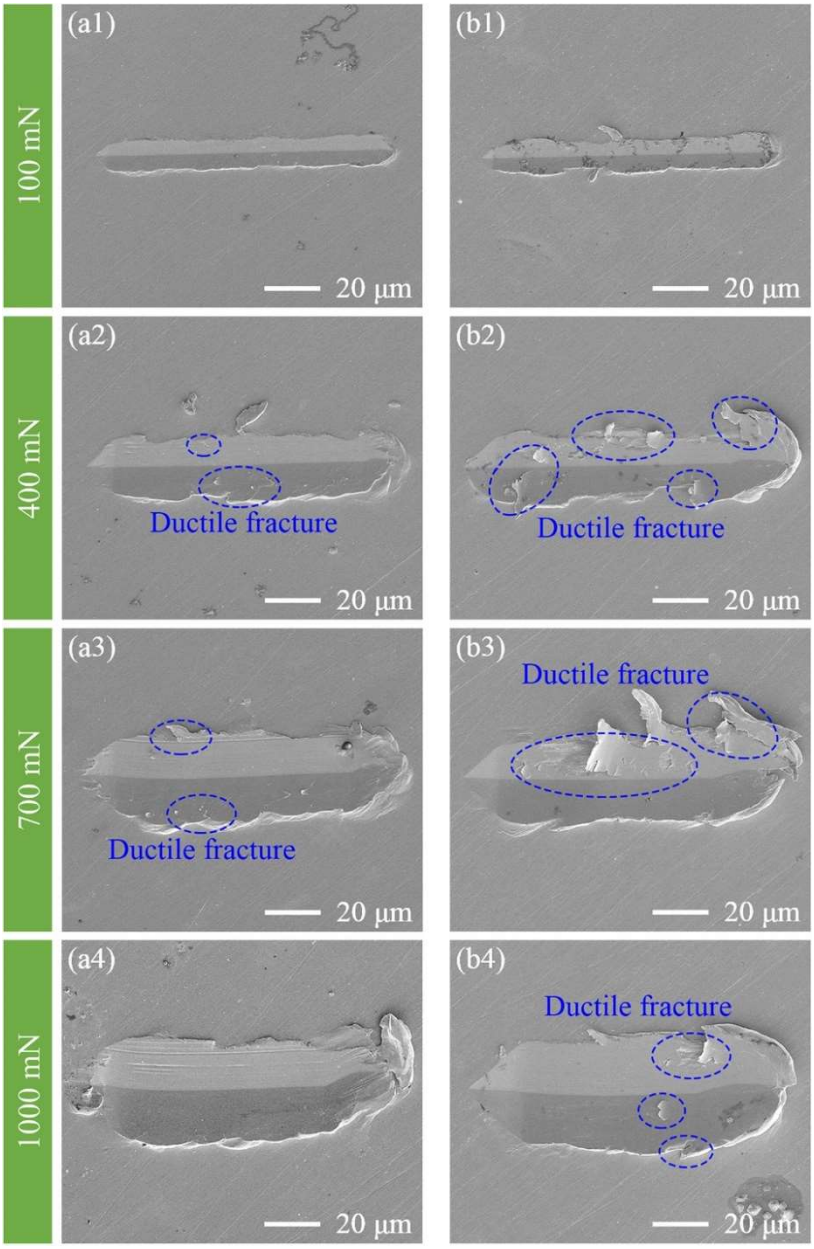

Figure 3. 2D scratched morphologies obtained under different loads: (**a1**–**a4**) without CPJ treatment; (**b1**–**b4**) under CPJ treatment.

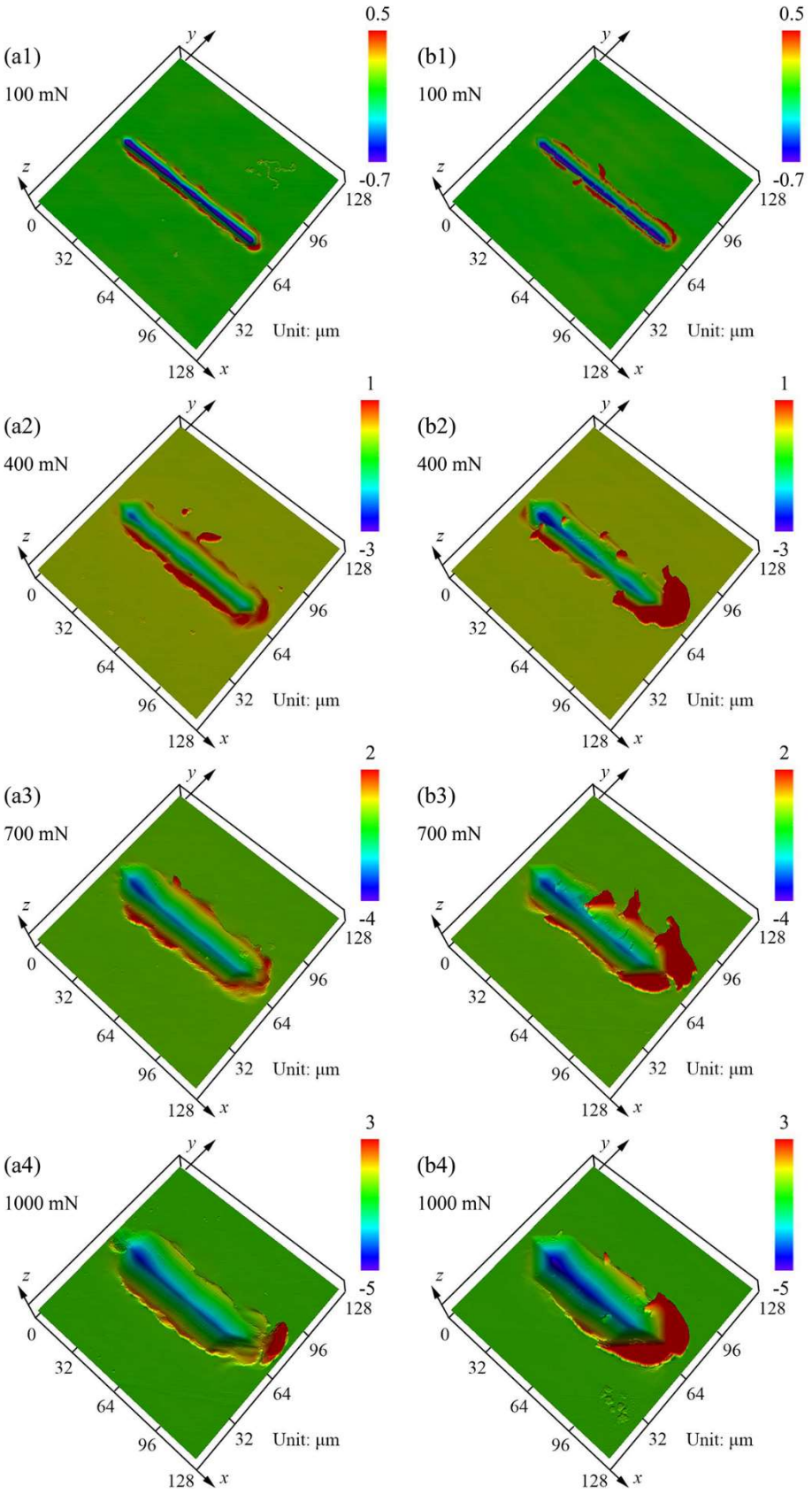

Figure 4. 3D scratched morphologies obtained under different loads: (**a1**–**a4**) without CPJ treatment; (**b1**–**b4**) under CPJ treatment.

The residual scratched depth under different loads was measured along the scratched cross-section direction, as shown in Figure 5. Case 1 and Case 2 represent the samples before and after CPJ treatment, respectively. Compared without CPJ treatment, it was found that the residual depth increased after CPJ treatment, and the scratched cross-sectional area also increased. To comprehensively evaluate the removal efficiency of the material before and after CPJ treatment, the parameter *R* was introduced to calculate the material removal efficiency, which was defined as [40]:

$$R = \left(S_2 - S_1\right) / S_2 \tag{1}$$

where S_1 was the area due to plastic pileups of the material, i.e., the area enclosed by the scratched profile curve above the depth baseline (depth = 0) and the baseline, and S_2 was the area of the scratched groove cross-section, i.e., the area enclosed by the scratched profile curve below the depth baseline and the baseline. The schematic diagram about S_1 and S_2 is shown in Figure 6a. The material removal efficiency reflected the combined effects of ploughing and ductile removal during the scratching process. For ductile removal, R ranges from 0–1. A larger value of R implied a greater proportion of ductile removal and a higher material removal efficiency during the scratching process. The material removal efficiency with and without CPJ treatment under different loads is shown in Figure 6b. The results suggested that after CPJ treatment, the material removal efficiency was greatly improved under each load, and the value of R at 400 mN was increased from 0.433 before treatment to 0.895. Combined with the results of the variable-load scratching test, it could be seen that this was because plasma could promote material fracture through the Rehbinder effect, which could promote the increase of scratched depth and material removal efficiency at the same load. At the same time, the friction coefficient μ during the scratching process was calculated, and the equation was:

$$\mu = F_L / F_N \tag{2}$$

where F_L and F_N were the lateral force and normal force, respectively. The friction coefficient under different loads is shown in Figure 6c. Compared with before CPJ treatment, the friction coefficient of the material after treatment increased under each load. The increase in friction coefficient could improve the material removal efficiency to a certain extent [41–43], which was also an important reason for the increase in material removal efficiency under CPJ-assisted scratching.

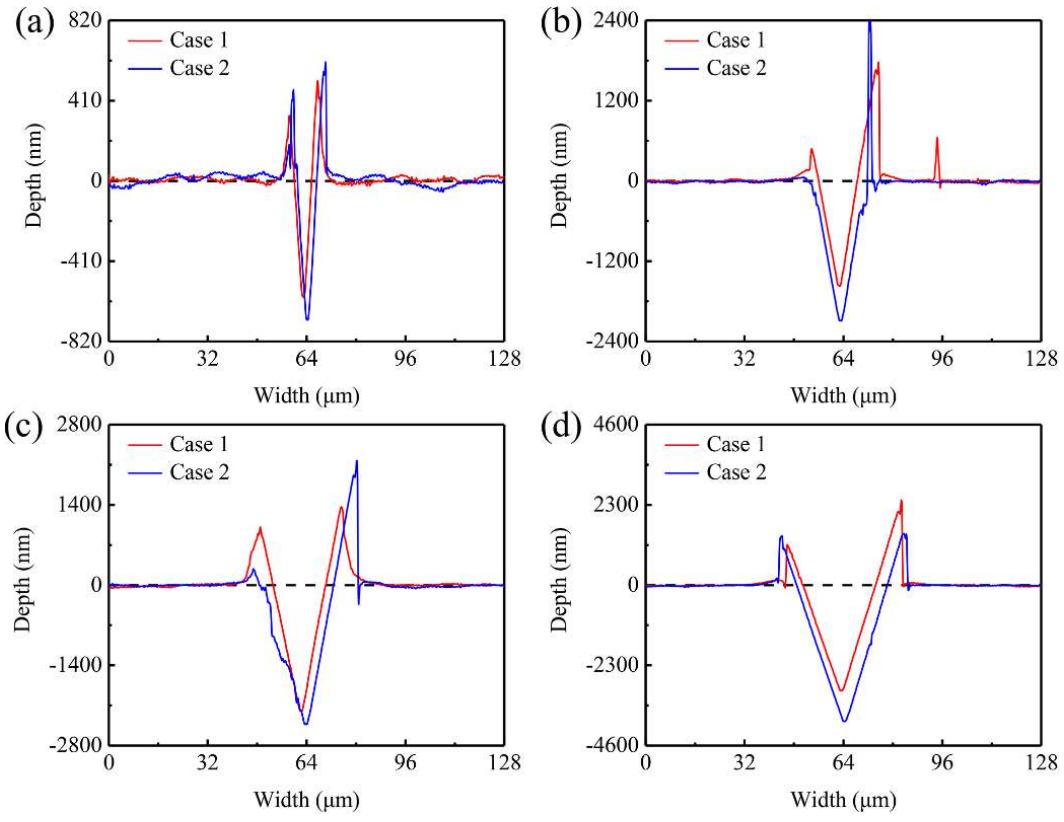

Figure 5. Residual scratched depth at different loads: (**a**) 100 mN; (**b**) 400 mN; (**c**) 700 mN; (**d**) 1000 mN.

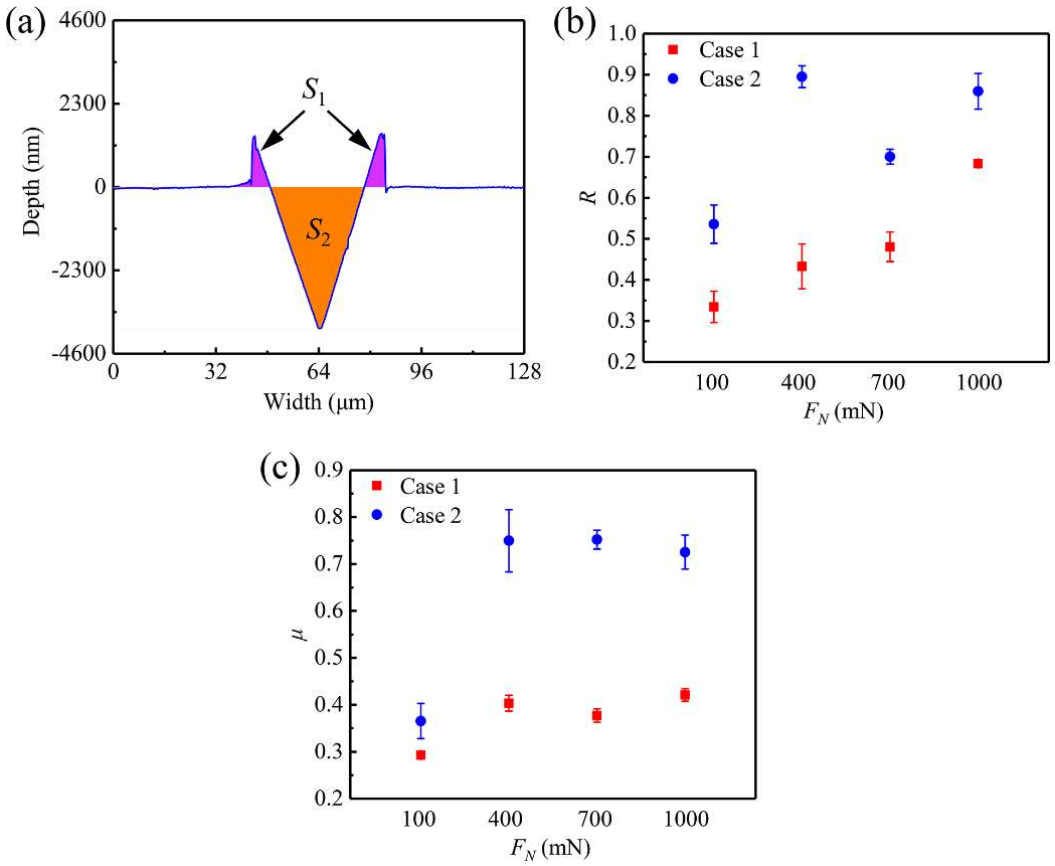

Figure 6. Material removal efficiency and friction coefficient with and without CPJ assistance at different loads: (**a**) schematic diagram on the definition of removal efficiency; (**b**) material removal efficiency at different loads; (**c**) friction coefficient at different loads.

3.2. The Exploration of Optimal Processing Parameters

To obtain the optimal processing parameters for dry micro-milling of 30CrMnSiNi2A, the orthogonal micro-milling experiment was carried out on the material. The optimal processing parameters were selected based on the surface roughness *Sa* and the cutting forces along all directions. A new tool was used in each milling test to avoid the influence of tool wear on the experiment results.

3.2.1. The Design of Orthogonal Experiment

The experiment mainly considered three factors: feed speed (V_f), spindle speed (n) and milling depth (a_p), so the experiment was a three-factors four-levels, i.e., L_{16} (4^3) orthogonal experiment. The tables of orthogonal experiment factor level and orthogonal experiment are shown in Table 5 and Table 6, respectively.

Table 5. Factor level table of orthogonal experiment.

Level	Factors		
	A/V_f (μm/s)	**B/n (10^4 rpm)**	**C/a_p (μm)**
1	200	2	5
2	500	3	10
3	800	4	15
4	1100	5	20

Table 6. Table of orthogonal experiment.

NO.	Factors		
	A	**B**	**C**
1	A1 (200)	B1 (2)	C1 (5)
2	A1	B2 (3)	C2 (10)
3	A1	B3 (4)	C3 (15)
4	A1	B4 (5)	C4 (20)
5	A2 (500)	B1	C2
6	A2	B2	C1
7	A2	B3	C4
8	A2	B4	C3
9	A3 (800)	B1	C3
10	A3	B2	C4
11	A3	B3	C1
12	A3	B4	C2
13	A4 (1100)	B1	C4
14	A4	B2	C3
15	A4	B3	C2
16	A4	B4	C1

3.2.2. The Results of Orthogonal Experiment

As shown in Figure 7a, the surface roughness *Sa* and cutting forces along all directions under each experiment were measured. Among the *Sa* obtained under each experiment, the *Sa* of 0.045 μm obtained by the processing parameters of NO. 11 (V_f = 800 μm/s, n = 40,000 rpm, and a_p = 5 μm) was the smallest. Meanwhile, it could be seen that the cutting forces along directions of x, y, and z obtained in NO. 11 were all small by observing the cutting forces in Figure 7b–d. Therefore, the processing parameters of V_f = 800 μm/s, n = 40,000 rpm, and a_p = 5 μm were selected for the subsequent micro-milling experiment under different working conditions.

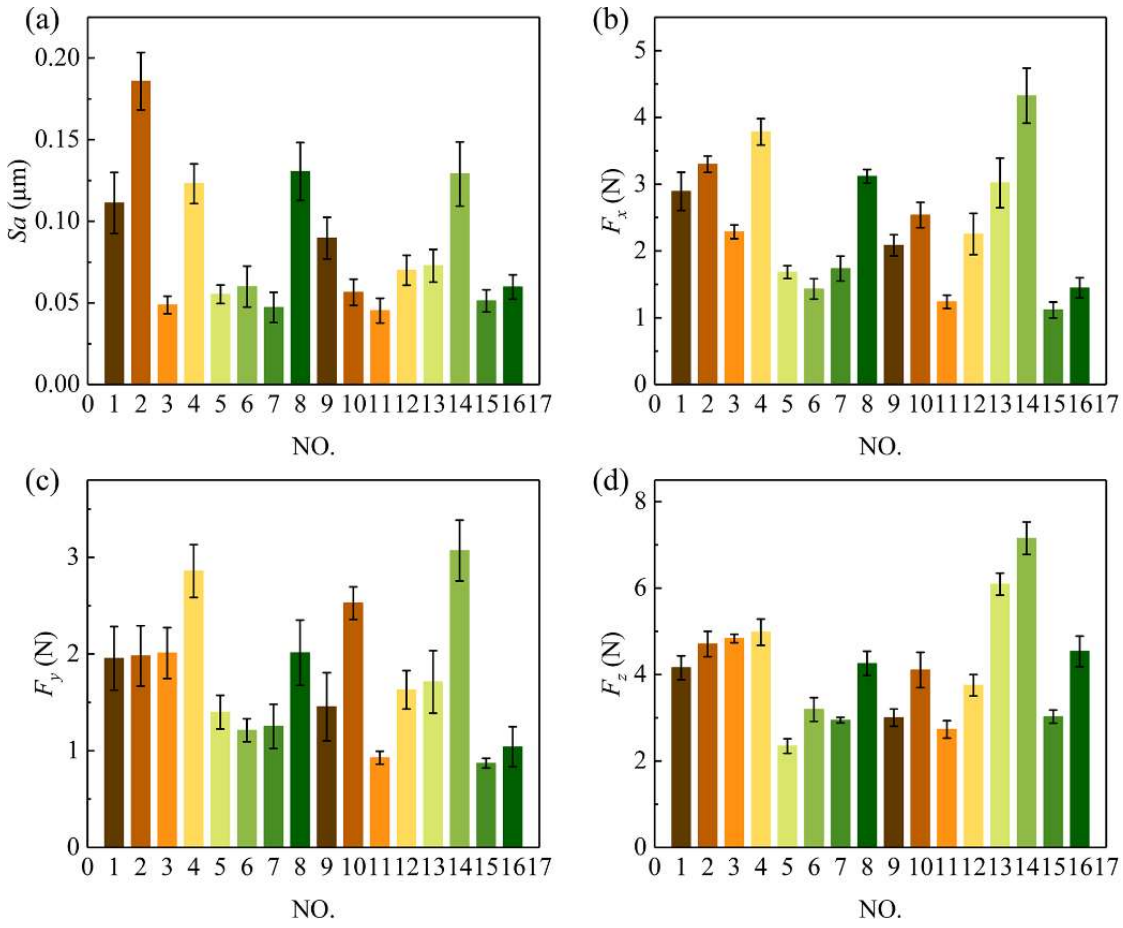

Figure 7. Surface roughness and cutting force obtained from orthogonal experiment: (**a**) surface roughness; (**b**–**d**) cutting force, (**b**) along x direction, (**c**) along y direction, (**d**) along z direction.

3.2.3. The Data Analysis of Orthogonal Experiment

The machined surface roughness *Sa* and the cutting force along *z* direction F_z were used as comprehensive measurement indicators for data analysis of orthogonal experiment. The signal noise ratio (SNR) was utilized to characterize the measurement indicators, where $\eta_S(n)$ and $\eta_F(n)$ represented the SNR of *Sa* and F_z in each experiment number *n* (*n* = 1, 2, 3, …16), respectively. The calculation equations were as follows:

$$\eta_S(n) = -10\log_{10}(Sa)^2 \tag{3}$$

$$\eta_F(n) = -10\log_{10}(F_z)^2 \tag{4}$$

After calculation by Equation (3) and Equation (4), the SNR results are shown in the Table 7.

Table 7. The SNR calculation results of *Sa* and F_z in each experiment.

NO.	Factors			Experimental Results			
	A	B	C	*Sa* (μm)	F_z (N)	η_S/dB	η_F/ dB
1	A1 (200)	B1 (2)	C1 (5)	0.111	4.157	19.094	−12.376
2	A1	B2 (3)	C2 (10)	0.186	4.708	14.610	−13.457
3	A1	B3 (4)	C3 (15)	0.049	4.834	26.196	−13.686
4	A1	B4 (5)	C4 (20)	0.123	4.982	18.202	−13.948
5	A2 (500)	B1	C2	0.055	2.347	25.193	−7.410
6	A2	B2	C1	0.060	3.194	24.437	−10.087
7	A2	B3	C4	0.047	2.944	26.558	−9.379
8	A2	B4	C3	0.131	4.257	17.655	−12.582
9	A3 (800)	B1	C3	0.090	3.002	20.915	−9.548
10	A3	B2	C4	0.057	4.105	24.883	−12.266
11	A3	B3	C1	0.045	2.731	26.936	−8.726
12	A3	B4	C2	0.070	3.753	23.098	−11.488
13	A4 (1100)	B1	C4	0.073	6.091	22.734	−15.694
14	A4	B2	C3	0.129	7.153	17.788	−17.090
15	A4	B3	C2	0.051	3.026	25.849	−9.617
16	A4	B4	C1	0.060	4.537	24.437	−13.135

To further analyze the influence of various factors on *Sa* and F_z, the mean and range of SNR of each factor were calculated. The means of SNR for each factor at each level *i* (*i* = 1, 2, 3, 4) were calculated as follows:

$$K_S(i) = \frac{1}{4}\sum \eta_s(n) \tag{5}$$

$$K_F(i) = \frac{1}{4}\sum \eta_F(n) \tag{6}$$

where *n* was the experiment number corresponding to the *i*-th level. The range equations of SNR under each factor were:

$$R_S = \max(K_S(i)) - \min(K_S(i)) \tag{7}$$

$$R_F = \max(K_F(i)) - \min(K_F(i)) \tag{8}$$

From Equations (5)–(8), the calculation results about mean and range of SNR are shown in Table 8. From the data in Table 8, it could be concluded that R_S(B) > R_S(A) > R_S(C). It implied that spindle speed had the greatest influence on *Sa*, followed by feed speed, and milling depth had the least influence of the three factors. In addition, it was obvious that R_F(A) > R_F(B) > R_F(C), which indicated that feed speed had the greatest influence on F_z, while spindle speed and milling depth had less influence on F_z.

Table 8. The calculation results about mean and range of SNR.

Results	Factors / Levels	A	B	C
		V_f (μm/s)	n (10^4 rpm)	a_p (μm)
$K_S(i)$	1	19.525	21.984	23.726
	2	23.461	20.429	22.187
	3	23.958	26.385	20.639
	4	22.702	20.848	23.094
R_S		4.433	5.955	3.087
$K_F(i)$	1	−13.367	−11.257	−11.081
	2	−9.864	−13.225	−10.493
	3	−10.507	−10.352	−13.227
	4	−13.884	−12.788	−12.822
R_F		4.020	2.873	2.734

3.3. The Effect of CPJ on Micro-Milling Process

To reveal the influence of CPJ on the cutting process, micro-milling experiments were carried out under three working conditions: dry, nitrogen and CPJ. A new tool was used for cutting in each condition, and the adopted processing parameters were the ones (V_f = 800 μm/s, n = 40,000 rpm, and a_p = 5 μm) obtained by orthogonal experiment. The cutting forces along each direction, surface roughness *Sa* and surface morphology were measured for analyzing the effect of CPJ on micro-milling process.

3.3.1. Cutting Force and Sa

As shown in Figure 8, compared with dry micro-milling, the cutting forces along the *z*, *x*, and *y* directions under CPJ-assisted micro-milling were reduced by 26.5%, 24.8% and 31.3%, respectively, which was very favorable for improving cutting conditions and slowing down tool wear. Meanwhile, the surface roughness was also improved, and *Sa* was reduced by 19.3%. Obviously, the cutting force and *Sa* under nitrogen were not significantly different from those under dry micro-milling, indicating that the active particles in CPJ improved the cutting process, rather than the airflow impact.

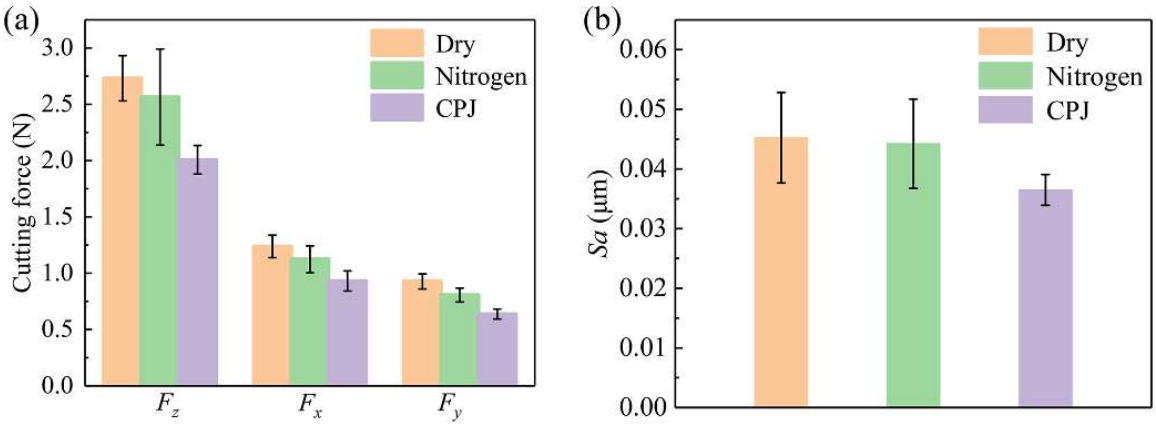

Figure 8. Cutting force and surface roughness under different working conditions: (**a**) cutting force along *z*, *x*, and *y* directions; (**b**) surface roughness *Sa*.

3.3.2. Surface Morphology

To further compare the differences in the surface morphology obtained under different working conditions, the 3D morphologies of the machined surface under three working conditions were measured, as shown in Figure 9(a1,b1) and (c1). Under dry and nitrogen working conditions, due to the plastic flow of the material, the tool marks on the machined surface were more serious. This was the plastic deformation phenomenon caused by the extrusion of the tool during the micro-milling process. At this time, the surface roughness *Sa* was also about 0.045 μm. After CPJ treatment, the plastic flow phenomenon on the material surface was significantly suppressed, and the tool marks on the machined surface were effectively alleviated, which greatly improved the surface quality. Simultaneously, the micromorphologies of the machined surface under different working conditions were measured, as shown in Figure 9(a2,b2,c2). Similar to the 3D morphologies, the micromorphologies of the machined surface under dry and nitrogen also exhibited plastic flow

phenomenon, and there were many burrs at the edges, which was due to the good toughness of the material, making it more difficult to break the burrs. Under CPJ-assisted micro-milling, the plastic flow phenomenon on the machined surface was significantly alleviated, and the burr phenomenon was also suppressed. In addition, there were many fragments on the machined surface, which might be related to the material fracture. It was also consistent with the results of the previous scratching test, that is, CPJ could regulate the mechanical properties of the material through the Rehbinder effect and thus promote material fracture.

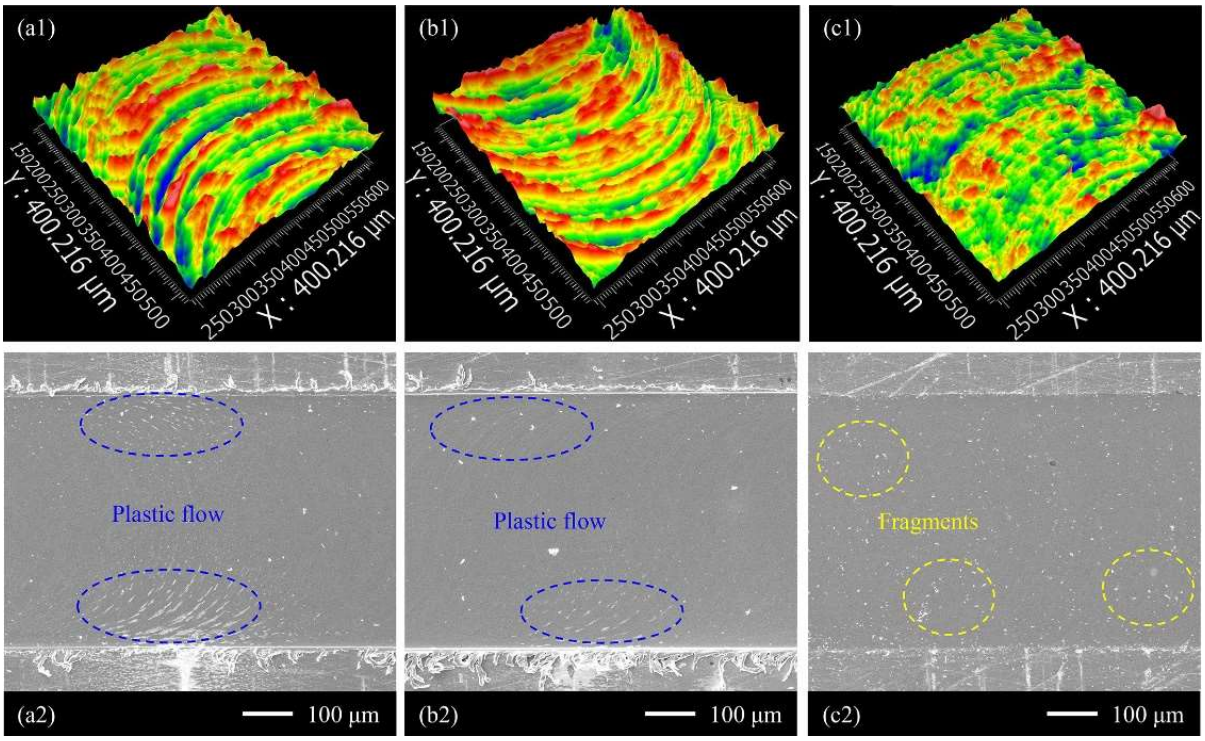

Figure 9. 3D morphologies and micromorphologies of the machined surface obtained under different working conditions: (**a1**,**a2**) dry; (**b1**,**b2**) nitrogen; (**c1**,**c2**) CPJ.

3.4. The Mechanism of CPJ-Assisted Micro-Milling 30CrMnSiNi2A

Based on the above effects of CPJ on material removal behavior and cutting process, the mechanism of CPJ-assisted micro-milling of 30CrMnSiNi2A was analyzed. The schematic diagram of the mechanism is shown in Figure 10. The Rehbinder effect was named after P.A. Rehbinder, who first reported this surface effect in 1928. In the study of the effects of surfactants on the properties of crystalline materials, Rehbinder found that surfactants could reduce the surface energy of the material, thereby reducing the hardness and fracture toughness of the material and promoting material fracture [44]. Subsequently, some scholars [45–47] investigated the Rehbinder effect and combined it with cutting processing, and the results suggested that the Rehbinder effect could effectively promote chip fracture and reduce cutting force, which was of great significance for improving material cutting processing. Therefore, containing a large number of active particles, CPJ could promote the ductile fracture of 30CrMnSiNi2A through the Rehbinder effect and inhibit plastic flow, and thus reduce cutting force and improve surface quality [48–50].

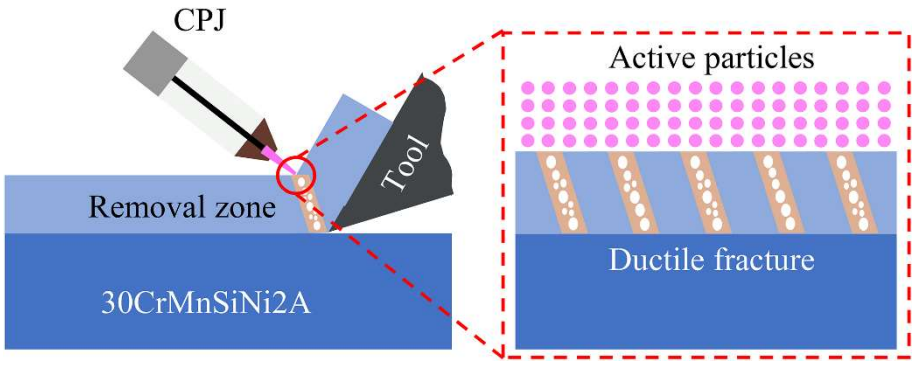

Figure 10. Schematic diagram of CPJ to improve 30CrMnSiNi2A machinability.

4. Conclusions

This paper proposed the utilization of CPJ to modulate the material properties of 30CrMnSiNi2A, and systematically studied the mechanism of CPJ on material properties and cutting process based on single-grain diamond scratching test and micro-milling test. The main conclusions of this paper are summarized as follows:

(1) In the single-grain diamond scratching test, CPJ could promote material fracture. The material removal efficiency R treated by CPJ was greatly improved under each load, and the value of R at 400 mN was increased from 0.433 before treatment to 0.895. The increase in friction coefficient after treatment was also an important reason for the significant increase in material removal efficiency.

(2) The surface roughness *Sa* of 0.045 μm obtained by the processing parameters of NO. 11 (feed speed V_f = 800 μm/s, spindle speed n = 40,000 rpm, and milling depth a_p = 5 μm) in the orthogonal experiment was the smallest. Meanwhile, the cutting forces in all directions were also small. The SNR analysis results manifested that the spindle speed had the greatest influence on *Sa*, and the feed speed had the greatest influence on F_z.

(3) Compared with dry micro-milling, the cutting forces F_z, F_x and F_y under CPJ-assisted micro-milling were reduced by 26.5%, 24.8% and 31.3%, respectively. It was very beneficial for improving cutting conditions and inhibiting tool wear. Additionally, the surface roughness *Sa* was reduced by 19.3%, and the phenomena of plastic flow and burr were significantly inhibited. The CPJ can regulate the material properties to improve the cutting process without causing serious damage to the material, and may have broad application prospects in the ultra-precision manufacturing of high-performance alloy materials such as 30CrMnSiNi2A.

Author Contributions

Conceptualization, Z.W. and X.L.; Methodology, Z.W.; Software, W.Y.; Validation, Z.D.; Formal Analysis, S.W.; Investigation, Z.W.; Resources, Y.L.; Data Curation, Y.Z.; Writing–Original Draft Preparation, Z.W.; Writing–Review & Editing, J.L., J.S. and X.L.; Visualization, Z.W.; Supervision, X.L.; Project Administration, X.L.; Funding Acquisition, X.L.

Ethics Statement

Not applicable.

Informed Consent Statement

Not applicable.

Funding

This work was financially supported by National Natural Science Foundation of China (Grant No.52475430), and the Fundamental Research Funds for the Central Universities (DUT23YG118).

Declaration of Competing Interest

The authors declare that they have no known competing financial interests or personal relationships that could have appeared to influence the work reported in this paper.

References

1. Zhang J, Jiang P, Zhu Z, Chen Q, Zhou J, Meng Y. Tensile properties and strain hardening mechanism of Cr-Mn-Si-Ni alloyed ultra-strength steel at different temperatures and strain rates. *J. Alloys Compd.* **2020**, *842*, 155856.
2. Duan Y, Liu W, Ma Y, Cai Q, Zhu W, Li J. Effect of Ni addition upon microstructure and mechanical properties of hot isostatic pressed 30CrMnSiNi2A ultrahigh strength steel. *Mater. Sci. Eng. A-Struct. Mater. Prop. Microstruct. Process.* **2022**, *850*, 143599.
3. Qi B, Wang M, Chu Z, Zhuang W, Zhou X, Zhao W, et al. Wear mechanism study of rocket sled shoe material 30CrMnSiNi2A. *Tribol. Int.* **2024**, *199*, 110003.
4. Wang L, Yu K, Cheng X, Cao T, Zhou L. Effect of laser shock peening on microstructure and mechanical properties of laser cladding 30CrMnSiNi2A high-strength steel. *Sci. Rep.* **2023**, *13*, 9971.
5. Klocke F, Soo SL, Karpuschewski B, Webster JA, Novovic D, Elfizy A, et al. Abrasive machining of advanced aerospace alloys and composites. *CIRP Ann-Manuf. Technol.* **2015**, *64*, 581–604.
6. Niu Q, Li P, Chen M, Ming W, Tang S. Analysis of chip serration phenomenon in side milling of ultrahigh-strength steel

30CrMnSiNi2A. *Int. J. Adv. Manuf. Technol.* **2017**, *88*, 985–993.
7. Niu Q, Dong D, Chen M, Zhang Y, Wang C. Dry milling of the ultra-high-strength steel 30CrMnSiNi2A with coated carbide inserts. *J. Shanghai Jiaotong Univ. (Sci.)* **2013**, *18*, 468–473.
8. Deng J, Song W, Zhang H. Design, fabrication and properties of a self-lubricated tool in dry cutting. *Int. J. Mach. Tools Manuf.* **2009**, *49*, 66–72.
9. Tuğrul Ö, Dirk B, Toshiyuki E, Paul M. Structured and textured cutting tool surfaces for machining applications. *CIRP Ann-Manuf. Technol.* **2021**, *70*, 495–518.
10. Shi Y, Zhao B, Ding W. Solid additives to increase the service life of ceramic cutting tool: Methodology and mechanism. *Intell. Sustain. Manuf.* **2024**, *1*, 10009.
11. Pang K, Wang D. Study on the performances of the drilling process of nickel-based superalloy Inconel 718 with differently micro-textured drilling tools. *Int. J. Mech. Sci.* **2020**, *180*, 105658.
12. Li B, Li C, Zhang Y, Wang Y, Jia D, Yang M. Grinding temperature and energy ratio coefficient in MQL grinding of high-temperature nickel-base alloy by using different vegetable oils as base oil. *Chin. J. Aeronaut.* **2016**, *29*, 1084–1095.
13. Wang X, Li C, Zhang Y, Ali HM, Sharma S, Li R, et al. Tribology of enhanced turning using biolubricants: A comparative assessment. *Tribol. Int.* **2022**, *174*, 107766.
14. Xu W, Li C, Cui X, Zhang Y, Yang M, Gao T, et al. Atomization mechanism and machinability evaluation with electrically charged nanolubricant grinding of GH4169. *J. Manuf. Process.* **2023**, *106*, 480–493.
15. ZHANG Y, LI L, CUI X, AN Q, XU P, WANG W, et al. Lubricant activity enhanced technologies for sustainable machining: Mechanisms and processability. *Chin. J. Aeronaut.* **2024**. doi:10.1016/j.cja.2024.08.034.
16. Maruda RW, Szczotkarz N, Michalski M, Arkusz K, Wojciechowski S, Niesłony P, et al. Evaluation of tool wear during turning of Ti6Al4V alloy applying MQL technique with Cu nanoparticles diversified in terms of size. *Wear* **2023**, *532–533*, 205111.
17. You H, Zhao B, Ding W, Miao Q, Yang C, Zhao Y, et al. Wear behavior of white alumina and seeded gel abrasive wheels in ultrasonic vibration-assisted grinding of nickel-based single-crystal alloy. *Wear* **2024**, *556–557*, 205505.
18. Xiang D, Sang J, Peng P, Yuan Z, Song C, Liu G, et al. Friction characterization of SiCp/Al composites by 3D ultrasonic vibration-assisted milling. *Mech. Syst. Signal Proc.* **2024**, *212*, 111302.
19. Wang C, Chen J, Zhang X, Wang T, Yang L, An Q, et al. Effects of ultrasonic vibration assisted milling with laser ablation pretreatment on fatigue performance and machining efficiency of SiCf/SiC composites. *J. Eur. Ceram. Soc.* **2023**, *43*, 5925–5939.
20. Huang K, Shen Z, Zheng Z, Lin C, Huang W, Zhang J, et al. Investigation on the machinability of nitriding mold steel by applying in-situ laser assisted diamond cutting. *J. Manuf. Process.* **2022**, *84*, 149–161.
21. Panjehpour A, Soleymani Yazdi MR, Shoja-Razavi R. An experimental investigation of pulsed laser-assisted machining of AISI 52100 steel. *Opt. Laser Technol.* **2014**, *63*, 137–143.
22. Du Y, Lu M, Lin J, Li Y, Sun S. Investigation on machinability of SiCp/Al composites under the synergistic effect of pulsed laser assisted and ultrasonic elliptical vibration cutting. *J. Mater. Process. Technol.* **2024**, *332*, 118561.
23. Gu G, Wang D, Wu S, Zhou S, Zhang B. Research Status and Prospect of Ultrasonic Vibration and Minimum Quantity Lubrication Processing of Nickel-based Alloys. *Intell. Sustain. Manuf.* **2024**, *1*, 10006.
24. Ji J, Cui X, Ma J, Zhou H, Xiang D, Ming P. Grafting–inspired bionic hierarchical structure for efficiently enhancing cemented carbide tool performance in green turning. *J. Mater. Process. Technol.* **2024**, *324*, 118274.
25. An Q, Yang J, Li J, Liu G, Chen M, Li C. A state-of-the-art review on the intelligent tool holders in machining. *Intell. Sustain. Manuf.* **2023**, *1*, 10002.
26. Buchanan M. Everything is plasma. *Nat. Phys.* **2016**, *12*, 394.
27. Feng S, Zhang P, Zhang Y, Cao J, Zheng Y, Wang J, et al. Self-cleaning transparent photovoltaic device in perovskite SrTiO3 quantum dot modified CuGaO2/Zn2SnO4 nanoarrays pn junction via surface plasma modification. *Appl. Phys. Lett.* **2024**, *125*, 091902.
28. Aggelopoulos CA. Recent advances of cold plasma technology for water and soil remediation: A critical review. *Chem. Eng. J.* **2022**, *428*, 131657.
29. Fang Z, Zhang Y, Li R, Liang Y, Deng H. An efficient approach for atomic-scale polishing of single-crystal silicon via plasma-based atom-selective etching. *Int. J. Mach. Tools Manuf.* **2020**, *159*, 103649.
30. Sun R, Yang X, Arima K, Kawai K, Yamamura K. High-quality plasma-assisted polishing of aluminum nitride ceramic. *CIRP Ann-Manuf. Technol.* **2020**, *69*, 301–304.
31. Liu N, Sugimoto K, Yoshitaka N, Yamada H, Sun R, Kawai K, et al. Effects of polishing pressure and sliding speed on the material removal mechanism of single crystal diamond in plasma-assisted polishing. *Diam. Relat. Mater.* **2022**, *124*, 108899.
32. Mustafa G, Liu J, Zhang F, Wang G, Yang Z, Harris M, et al. Atmospheric pressure plasma jet assisted micro-milling of Inconel 718. *Int. J. Adv. Manuf. Technol.* **2019**, *103*, 4681–4687.
33. Liu J, Song J, Chen Y, Zhang J, Wu L, Wang G, et al. Atmospheric pressure cold plasma jet–assisted micro-milling TC4 titanium alloy. *Int. J. Adv. Manuf. Technol.* **2021**, *112*, 2201–2209.
34. Liu X, Wang B, Li Y, Zhou Y, Zhang J, Wang Z, et al. Improving machinability of single-crystal silicon by cold plasma jet. *J. Manuf. Process.* **2023**, *99*, 581–591.

35. Wang Z, Li Y, Wang S, Duan Z, Cao X, Zhou Y, et al. Feasibility and mechanism of atmospheric pressure cold plasma jet (APCPJ) assisted micro-milling of bulk metallic glasses (BMGs). *Ceram. Int.* **2024**, *50*, 11094–11105.
36. Duan Z, Wang S, Wang Z, Li C, Li Y, Song J, et al. Tool wear mechanisms in cold plasma and nano-lubricant multi-energy field coupled micro-milling of Al-Li alloy. *Tribol. Int.* **2024**, *192*, 109337.
37. Duan Z, Wang S, Li C, Wang Z, Bian P, Sun J, et al. Cold plasma and different nano-lubricants multi-energy field coupling-assisted micro-milling of Al-Li alloy 2195-T8 and flow rate optimization. *J. Manuf. Process.* **2024**, *127*, 218–237.
38. Wu H, Huang H, Xu Z, Li X, Zhao H. Development of a Vibration-Assisted Micro/Nano Scratch Tester for Evaluating the Scratch Behaviors of Materials Under Vibration Environment. *IEEE T. Ind. Electron.* **2024**, *71*, 15190–15199.
39. Boban J, Ahmed A. Effect of material composition on the action of surface active medium in ultra-precision microcutting. *Procedia CIRP* **2024**, *123*, 244–249.
40. He Y, Xiao G, Zhu S, Liu G, Liu Z, Deng Z. Surface formation in laser-assisted grinding high-strength alloys. *Int. J. Mach. Tools Manuf.* **2023**, *186*, 104002.
41. Hirano K, Sato T, Suzuki N. Real-time prediction of material removal rate for advanced process control of chemical mechanical polishing. *CIRP Ann-Manuf. Technol.* **2024**, *73*, 269–272.
42. Tian Y, Ma Z, Ma X, Li L, Yan J. A cross-scale material removal prediction model for magnetorheological shear thickening polishing. *J. Mater. Process. Technol.* **2024**, *332*, 118569.
43. Wei C, He C, Chen G, Sun Y, Ren C. Material removal mechanism and corresponding models in the grinding process: A critical review. *J. Manuf. Process.* **2023**, *103*, 354–392.
44. Rebinder PA. Influence of changes in the surface energy on cleavage, hardness, and other properties of crystals. In the Proceedings of the Sixth Conference of Russian Physicists, Moscow, Russia, 15 August 1928.
45. Fedorov AA, Blesman AI, Postnikov DV, Polonyankin DA, Russkikh GS, Linovsky AV. Investigation of the impact of Rehbinder effect, electrical erosion and wire tension on wire breakages during WEDM. *J. Mater. Process. Technol.* **2018**, *256*, 131–144.
46. Chaudhari A, Soh ZY, Wang H, Kumar AS. Rehbinder effect in ultraprecision machining of ductile materials. *Int. J. Mach. Tools Manuf.* **2018**, *133*, 47–60.
47. Lee YJ, Wang H. Current understanding of surface effects in microcutting. *Mater. Des.* **2020**, *192*, 108688.
48. Liu J, Wang S, Li Y, Duan Z, Ning L, Wang Z, et al. High-efficiency and low-damage modification of engineering metal materials by oxygen-mixing atmospheric pressure cold plasma jets. *Appl. Surf. Sci.* **2024**, *662*, 160142.
49. Duan Z, Wang S, Li C, Wang Z, Bian P, Song J, et al. Performance evaluation of cold plasma and h-BN nano-lubricant multi-field coupling assisted micro-milling of aluminum alloy 6061-T651. *Alex. Eng. J.* **2024**, *109*, 610–625.
50. Liu J, Li Y, Chen Y, Zhou Y, Wang S, Yuan Z, et al. A review of low-temperature plasma-assisted machining: From mechanism to application. *Front. Mech. Eng.* **2023**, *18*, 18.